Raster angle impact on FDM-based additive manufactured fluidic oscillator

16 (2022) 100230

Contents lists available at ScienceDirect

International Journal of Thermofluids

journal homepage: www.elsevier.com/locate/ijtf

Raster angle impact on FDM-based additive manufactured fluidic oscillator

Abdul Raouf Tajik [a,b], Tauha Irfan Khan [a], Vladimir Parezanović [a,*]

[a] Aerospace Engineering Department, Khalifa University of Science and Technology, P.O. Box 127788, Abu Dhabi, United Arab Emirates
[b] Division of Fluid Dynamics, Department of Mechanics and Maritime Sciences, Chalmers University of Technology, 412 96 Gothenburg, Sweden

ARTICLE INFO

Keywords:
Fluidic oscillator
Sweeping jet actuator
Additive manufacturing
Fused Deposition Modeling
Raster angle
Surface texture

ABSTRACT

The interior surface of a fluidic oscillator produced by FDM (Fused Deposition Modeling)-based additive manufacturing is associated with a directional pattern corresponding to the 3D printing raster angle. The present research explores the impact of raster angle $\alpha = 0$, 45, and 90° from three commercial 3D printers versus a CNC machined oscillator. The surface is characterized using an optical 3D measurement system. The performance of the emanated jet is assessed using hot-wire anemometry downstream of the outlet nozzle, and the required supply pressure is measured at the actuator inlet. Printer P_1 with an actuator average roughness $\bar{S}_a = 8.3$ μm and printer P_2 with $\bar{S}_a = 29.9$ μm inherit clear raster patterns while actuators printed by printer P_3, more economical compared to printer P_1, do not exhibit an evident pattern related to raster angle with $\bar{S}_a = 17.7$ μm. Regardless of the type of printer and associated surface texture, oscillators with 0° raster angle provoke higher jet spreading accompanied by a lower required supply pressure compared to the milled sample. Strikingly, the performance for P_3^0 and P_3^{90} is noticeably superior to the other printed oscillators and surpasses the milled actuator in terms of jet switching quality. Power-law fit is depicted to estimate the jet spreading versus surface roughness for each raster angle.

1. Introduction

Additive manufacturing (AM) and 3D printing technologies will revolutionize the manufacturing of fluidic systems and heat exchangers by enabling innovative design and development of sensors and actuators in a wide range of engineering applications [1–4]. Among the actuators, fluidic oscillators of different types and designs have attracted much attention and are advantageous since they are easy to fabricate and do not involve moving parts. The fluidic oscillator has been widely studied for several engineering applications such as separation control [5] and combustion control [6] to minimize the pollutants emission from exothermic reactive flows [7–11]. In the last few decades, attempts have been made to make transport mediums more sustainable and energy efficient [12]. It is well-known that the turbulent wake aft of flat-back bluff bodies is characterized by massive separation resulting in large pressure drag and increased vehicle fuel consumption [13,14]. Sweeping jet actuators (SWJ) have been increasingly popular in the exploration of drag reduction, and have been applied to various generic models of terrestrial vehicles [15–18].

Synthetic and steady jets have been widely studied for flow control and heat transfer enhancement [19–26]. The unsteady characteristics of fluidic oscillators are desirable for the development of next-generation heat exchangers with extremely high heat flux removal capacity [27–29]. The heating uniformity index is a critical factor in heat transfer applications [30–32]. The sweeping jet yields more uniform heat removal performance due to a remarkably higher jet spreading than the plain jet [33]. The basic working principle of such an actuator is to provoke and harness a bi-stable internal flow. Bi-stable flows are ubiquitous in many fields of fluid engineering; they can occur in strongly separated three-dimensional flows [34–36], between separation and re-attachment, as in different arrangements of two-dimensional cylinders [37], in heat transfer [38,39], and flow control with a second smaller cylinder [40].

Recently additive manufacturing has been widely used to produce sweeping actuators [41,42]. It is well established that 3D printing inherits a noticeably complex surface finish [43] which impacts the performance of any thermofluidic system, including a fluidic oscillator [14,44]. Among various additive manufacturing technologies, fused deposition modeling (FDM) is the most widely used technique for fabricating prototypes and functional parts in common engineering plastics [45]. In the FDM-based printing technology, the deposition process involves the build materials in the form of a filament, which is exposed to heat and extruded from a temperature-controlled nozzle in a semi-liquid state. This filament is extruded in ultra-thin layers from the extrusion head, which moves along x and y axes to print the 2-D layer pattern of the object. The quality of the out-coming printed parts

* Corresponding author.
E-mail addresses: abdulraouf.tajik@chalmers.se (A.R. Tajik), vladimir.parezanovic@ku.ac.ae (V. Parezanović).

https://doi.org/10.1016/j.ijft.2022.100230
Received 23 July 2022; Received in revised form 24 September 2022; Accepted 6 October 2022
Available online 19 October 2022

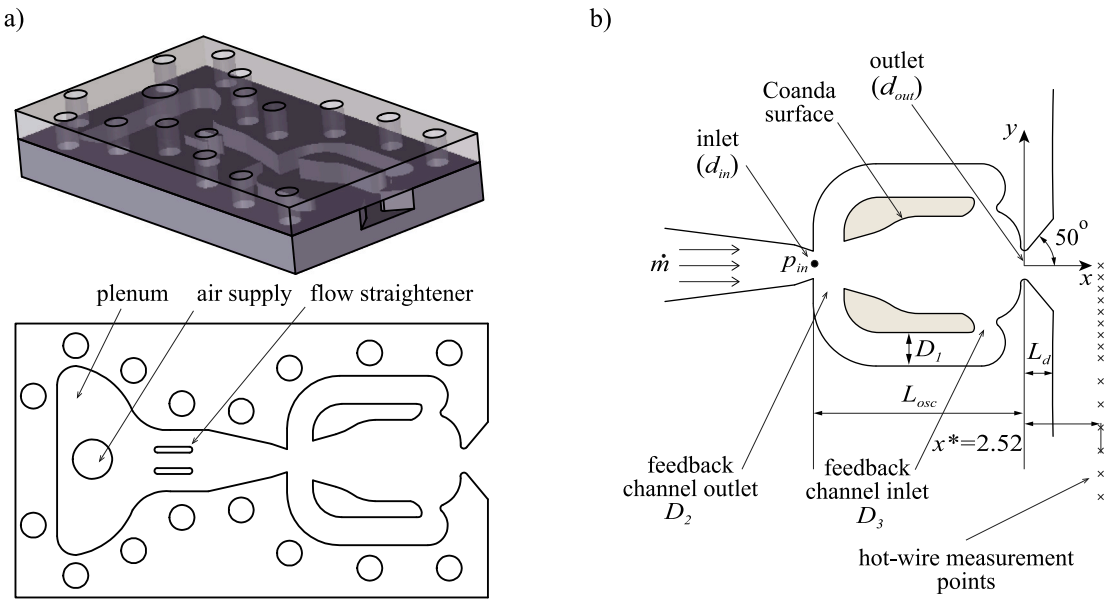

Fig. 1. (a) 3D model of the actuator with top cover assembled and at the bottom, the top view is depicted, and (b) A schematic of the curved sweeping jet actuator used in the experiment. Static pressure port locations are denoted with (•) and hot-wire measurement locations with (×) symbols.

is controlled by various printing parameters, such as the printing raster angle, the thickness of the layer, air gap, the orientation of printing, and raster width [46].

Raster angle is the angle of the raster tool path deposited with respect to the x-axis of the build table. Based on the size of the printer bed and the model reorientation, the printing raster angle can differ from one printer to the other despite using the same technology. It is well established that the raster angle significantly impacts the sample surface finish and its mechanical properties [47]. This research aims, from the thermofluids point of view, to address the effect of raster angle $\alpha = 0$, 45 and 90° from three different 3D printers versus the smooth machined sample on the flow and energy consumption of a sweeping jet actuator.

This article is structured as follows. The experimental setup, measurements, and production techniques are described in Section 2. In Section 3, we present the results and discussion with respect to the raster angle, and the concluding remarks are given in Section 4.

2. Experimental setup and measurements

The actuator design corresponds to a curved (also called Type-II) SWJ actuator with two feedback channels, as shown in Fig. 1. We used a machined aluminum plate as the top cover for all the tested samples. The main body and the cover are assembled using bolts and nuts. The working fluid is air, and the actuator expels the jet into a quiescent environment. Compressed air is supplied through a quick-connect adapter fastened to a threaded hole in the top aluminum plate (see Fig. 1b). The actuator inlet width is $d_{in} = 6.07$ mm. The actuator outlet throat width and the cavity depth are equal $d_{out} = h = 6.35$ mm, and therefore identical to the hydraulic diameter at the outlet $h = d_{out} = d_{hyd}$. The outlet nozzle half-angle is $\theta = 50°$, and the streamwise length of the diffuser is $L_d \approx 1.0h$ for all actuators in the experiment. Spatial coordinates x^* and y^* are dimensionless quantities with respect to the hydraulic diameter d_{hyd}.

2.1. Model manufacturing and surface characterization

The actuators used in these experiments vary in material and manufacturing process. Alicona Infinite Focus G5 is used to characterize the surface finish of each actuator. The most commonly used parameter to describe surface finish is the profile surface roughness R_a, which indicates the average of the absolute value of roughness profile along the sampling length, $R_a = 1/N \sum_{i=1}^{N} |z(x_i)|dx$ [48]. Although this parameter is widely utilized it cannot provide complete information on the three-dimensional surface structure, as in the case of a 3D printed actuator where the surface has random texture and is dominated by complex forms. Therefore, we use areal surface topography parameters, which are 3D in nature and are marked with the letter S [49]. According to ISO (International Organization for Standardization) 25178, ISO 12781-1, and ASME (the American Society of Mechanical Engineers) B46.1-2002, the areal surface roughness S_a can be calculated as the average height of the selected area:

$$S_a = \frac{1}{MN} \sum_{j=1}^{N} \sum_{i=1}^{M} |z(x_i, y_j)|dxdy \tag{1}$$

The Alicona Infinite Focus G5 has objective magnification of ×2.5 to ×100 and these provide lateral resolutions of 7.04 μm to 0.44 μm and vertical resolutions of 2.3 μm to 0.01 μm, respectively. We used ×50 objective for the milled actuator, and for the printed samples, since the surface is noticeably rougher, we used ×10. As shown in Fig. 2, we tested ten actuators, out of which one actuator is machined using the conventional milling process, and the other nine are additive manufactured using three different commercial FDM-based 3D printers at different raster angles. Fig. 2 illustrates the surface characteristics parameters for all the samples, and the areal surface roughness S_a is mentioned for each case. Fig. 2a depicts the parameters for the milled actuator. The surface height ranges ±1 μm evident from the height-map resulting in the areal surface roughness $S_a = 0.2$ μm. The PSD (Power Spectral Density) of the surface height versus the normalized spatial frequency f^* is presented, emphasizing the most dominant spatial frequency, which is the inverse of the wavelength of the roughness features. We can observe a prominent peak at around $f^* = 0.001$, corresponding to the cutting tool path.

Fig. 2b–d show the surface characterization parameters for the actuators 3D printed at different raster angles using three FDM-based printers. Printer P_1 is a Markforged Mark Two 3D printer, and Markforged 800cc Nylon is used as the filament deposition material. The STL files were sliced using Markforged Eiger software, an integrated platform designed to convert CAD files to functional parts. We used 0.2 mm as the deposition layer thickness and two shells with a triangular pattern with 50% infill density as recommended to avoid the sample

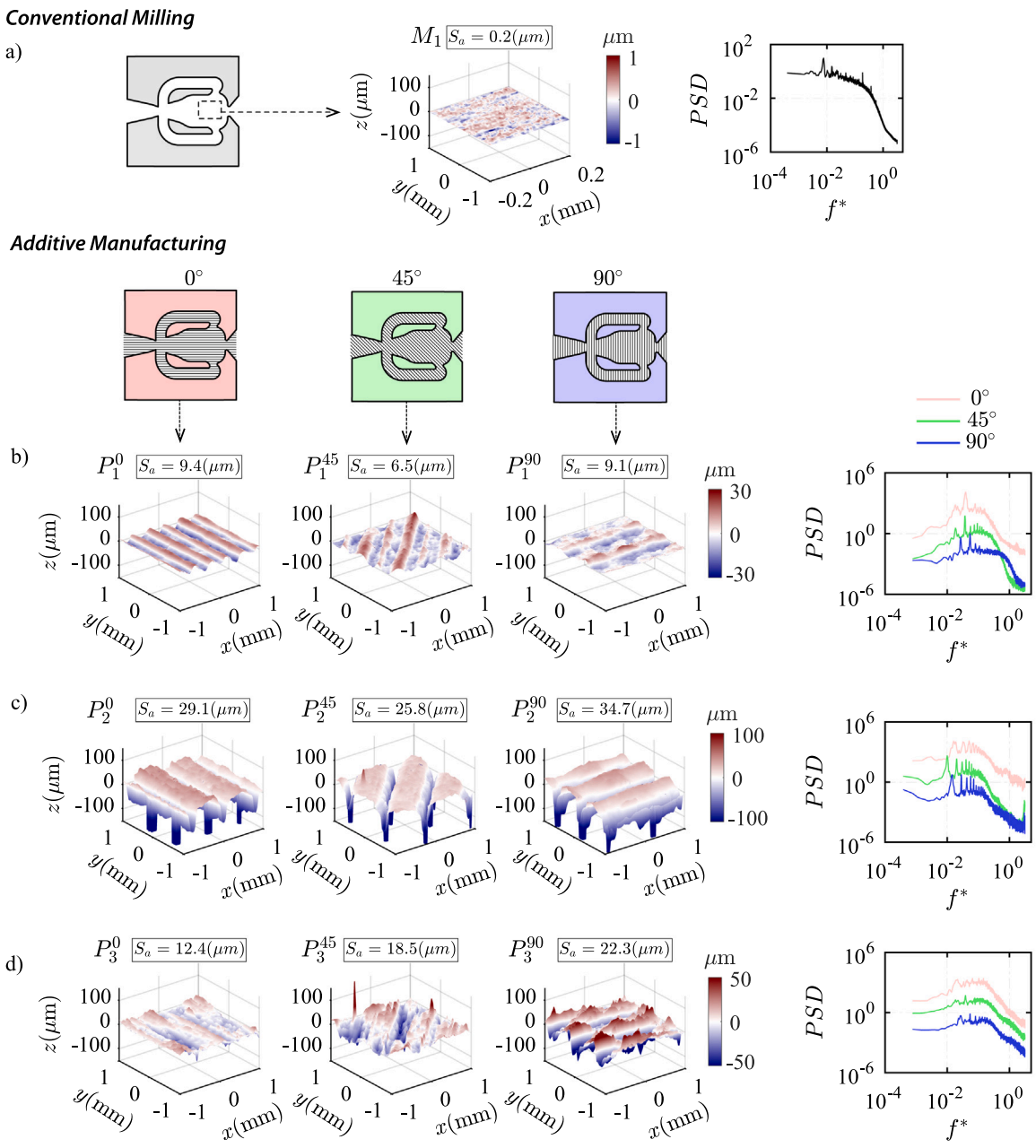

Fig. 2. The surface characteristics parameters: the height map $z(x, y)$ and PSD of surface height for (a) the milled actuator, (b) printer P_1: Markforged Mark-Two, (c) printer P_2: Sindoh 3DWOX-1, and (d) printer P_3: MakerBot Replicator+.

from warping at the sides. These settings are used for all the additive manufactured samples. For this printer, no support material was needed. The printing time has been 5 h and 20 min with a part mass of 59.8 g and material cost of 11.56 US$. The actuators are printed at three different raster angles P_1^0, P_1^{45}, and P_1^{90} by rotating the model. The air gap and raster/road width are not altered directly since the use of commercial software limits the user to change these parameters. The surface roughness S_a = 9.4, 6.5 and 9.1 μm for α = 0, 45 and 90° respectively. It is important to note that printer P_1 prints at 45° by default, and hence the surface roughness is lower for this raster angle. From PSD distribution, we can observe well-defined main frequency peaks corresponding to the raster direction.

Printer P_2 is a Sindoh 3DWOX-1 FDM-based 3D printer. The STL files were sliced with Sindoh 3DWOX Desktop software. Similarly, the samples are printed at three different raster angles P_2^0, P_2^{45}, and P_2^{90}. The printing time has been 8 h and 45 min, with a part mass plus support material of 77.5 g and the cost of 4.57 US$ which is noticeably more affordable than printer P_1. The surface roughness S_a = 29.4, 21.2 and 34.7 μm for α = 0, 45 and 90° respectively which are significantly rougher than the actuators printed by printer P_1. From the height maps, we can see a well-defined pattern concerning the raster angle, and also, the air gap is wider and deeper, which is the distance between two raster widths. We can also note eminent main frequency peaks from PSD distribution corresponding to the raster direction.

Finally, printer P_3 is a MakerBot Replicator+ 3D printer. The STL files were sliced with MakerBot Print open source software. The printing time has been 7 h and 49 min, with a part mass plus support material of 87.42 g with the cost of 4.85 US$, comparable to printer P_2. The samples are printed at three different raster angles P_3^0, P_3^{45}, and P_3^{90} with associated surface roughness S_a = 12.4, 18.5 and 22.3 μm. Unlike the other two printers, from the PSD distribution, prominent frequency peaks cannot be distinguished. In other words, as depicted by the height

Table 1
The relative percentage deviation in the main geometric dimensions normalized by the nominal dimensions (see Fig. 1).

	$\Delta Losc$	ΔD_1	ΔD_2	ΔD_3	Δh	Δd_{in}	Δd_{out}	S_a (μm)
$Milled$	0.0	−0.4	−0.4	−5.4	0.3	0.3	−0.2	0.2
P_1^0	0.0	−4.2	0.4	−4.3	0.9	7.0	2.3	9.4
P_1^{45}	0.0	−2.6	−1.0	−1.0	2.0	7.3	3.1	6.5
P_1^{90}	0.0	−3.6	−1.9	−2.3	1.1	7.0	2.6	9.1
P_2^0	0.0	−6.6	2.2	−0.8	−0.2	0.0	−2.4	29.1
P_2^{45}	−0.2	−1.4	0.0	−4.1	3.1	9.4	4.5	25.8
P_2^{90}	0.1	1.5	−6.7	−9.6	0.0	9.5	5.2	34.7
P_3^0	−0.2	−4.5	−1.5	−2.7	1.2	5.2	5.2	12.4
P_3^{45}	−0.1	−5.5	−0.6	−3.7	0.3	0.2	1.6	18.5
P_3^{90}	−0.2	−2.1	1.2	−1.7	0.8	1.3	5.2	22.3

maps, for printer P_3, the surface texture is not dominated by grooves corresponding to the raster direction, and the roughness distribution is randomly spread and does not obey the printing raster angle.

The dimensional accuracy of the printed samples is examined using Alicona Infinite Focus G5 measurement tool. Table 1 summarizes the relative deviation in the main geometric dimensions normalized by the true values $\Delta\psi = (\psi - \psi^{ref})/\psi^{ref} \times 100$. The deviation in the main geometric dimensions is mostly within ±5% for the milled and printed samples. The maximum deviation is noted for the inlet diameter where Δd_{in} reaches up to 9%. We shall elaborate further on these deviations in Section 3.2. The surface roughness value for each case is also shown in the last column.

2.2. Pressure and velocity measurements

A 7-bar compressed air source provides the pressurized air at a temperature of 25 °C. The inlet control parameter is the actuator mass flow rate $\dot{m}$, managed by an Alicat MCR-1500SLPM mass flow meter/controller. Mass flow rates used in the experiment ranged from 2 to 9 g/s, and the controller can maintain the desired value with a precision better than 0.1 g/s.

The internal required supply pressure is characterized by time-resolved local static pressure, measured using a Kulite XTL-140 high-frequency, absolute pressure transducer similar to in [50]. The transducer is mounted flush with the floor of the actuator at the throat of the power inlet p_{in} shown in Fig. 1. A National Instruments cDAQ™-917 data acquisition system is used to acquire data, with a sampling rate of $f_s = 10$ kHz and the acquisition period of $T = 10$ s.

External properties of the jet are evaluated using a TSI IFA-300 anemometer with a single hot-wire TSI Model 1211. A TSI model 1129 automatic calibrator was used to calibrate the hot wires over the range of 0–150 m/s, and a fourth-order polynomial was used to fit the velocity versus voltage curve. The typical uncertainty of the hot-wire velocity measurements across the entire range is less than 3%. The probe was mounted on a two-axis computer-controlled translation stage, enabling the wire to traverse in the xy−plane located at the middle of the cavity depth h at $z^* = 0$. The hot-wire is placed perpendicular to the xy−plane, measuring a modulus of velocity $U(t) = \sqrt{u^2(t) + v^2(t)}$ in that plane. In the further text, we represent the mean value of the velocity modulus as $\overline{U}$, and Root-Mean-Square (RMS) of its fluctuating part $U'(t) = U(t) - \overline{U}$ as U'_{rms}. The hot-wire measurements are obtained only for one-half of the span, with respect to the longitudinal axis of symmetry. For visualization purposes, the half-span velocity profiles are mirrored. Usually, the velocity profiles of SWJs are highly symmetric, however, in our case, we introduce asymmetry due to the oblique raster angle. In these cases, we have performed full-span velocity measurements for a few mass flow rates to verify that the velocity profiles do not exhibit a significant asymmetry. These velocity profiles are found to have only small asymmetry, and their impact on derived parameters such as the jet deflection angle θ can be considered negligible. As shown in Fig. 1, the measurements are acquired at 15 locations in the spanwise direction with the distance between two adjacent measurements $\Delta y = 2.5$ mm near the axis of the symmetry and $\Delta y = 5.0$ mm near the extremes of y^*. The data is acquired with a sampling rate of $f_s = 10$ kHz and the acquisition period of $T = 10$ s.

3. Results and discussions

The properties of the jet downstream of the exit nozzle are investigated using a stationary hot-wire probe as described in Section 2.2. The inlet velocity $\overline{U}_{in}$ of the actuator (see Fig. 1) is computed to be in the range of 44–151 m/s for the range of mass flow rates used in the experiment [44]. The associated maximum Mach number $M = \overline{U}_{in}/c$ is 0.46 for the mass flow rate of $\dot{m} = 9$ g/s. The Reynolds number at the inlet of the actuator is defined as $Re = \overline{U}_{in} d_{hyd}/\nu$. The Reynolds number is in a range of $1.8 \times 10^4 < Re < 8.5 \times 10^4$.

3.1. The CNC milled actuator

As explained in Section 2.1, to print the sample at different raster angles, the model had to be rotated to be compatible with the printer bed dimensions. As shown in Fig. 3, we had to shorten the entrance length L_e to 9.58 from 19.35 [51]. Therefore, before discussing the performance of the printed actuator, we characterize the milled sample. Fig. 3a–b depict the non-dimensional mean velocity $\overline{U}^*(y^*)$ and RMS velocity profiles $U'^*_{rms}(y^*)$ for $\dot{m} = 2$–9 g/s at $x^* = 2.52$ for $L_e = 9.58$ and $L_e = 19.35$ respectively. It is evident from the velocity profiles that the shorter actuator yield a lower spreading attributable to insufficient entrance length. This is interesting since, to the best of our knowledge, the effect of entrance length has not been studied, and arbitrary values of L_e were chosen for model fabrication.

We can extract several important performance parameters from the mean velocity profiles and PSD distribution of the velocity signals. Fig. 3c depicts the resulting performance parameters of the tested actuators with different entrance lengths. From the mean velocity profile in Fig. 3a, the jet half-width is quantified as δ, which is the y^* location where $\overline{U}(y^*) \geq 0.5\overline{U}_{max}(y^*)$ [52]. The jet half-width δ corresponds to the maximum jet deflection angle θ^*_{max} [52] as:

$$\theta^*_{max} = tan^{-1}\left(\frac{\delta}{x^*}\right) \times \frac{1}{\theta} = \frac{\theta_{max}}{\theta} \tag{2}$$

For the milled actuator with $S_a = 0.2$ μm (see Fig. 2) and $L_e = 9.58$, the average jet half-width $\delta = 3.13$ at $x^* = 2.52$, which corresponds to $\theta^*_{max} \approx 1.01$ that is lower by an average of 8% compared to $L_e = 19.35$. Therefore, the entrance length $L_e = 9.58$ seem to be insufficient, and hence, as compared to the longer actuator, the jet does not feature a clear twin peak profile expected from this group of oscillators. We shall discuss this further in Section 3.2.

The time-averaged required supply pressure is expressed as $p_s = \overline{p}_{in} - \overline{p}_\infty$ and is often used as an indicator of the actuator's overall energy consumption [51,53]. The standard deviation of p_s is less than ±3%, regardless of the mass flow rate. We present non-dimensional required supply pressure $p^*_s = p_s/q_{in}$ where $q_{in} = 0.5\rho\overline{U}^2_{in}$, and $1.20 < \rho < 1.53$ kg/m^3. Fig. 3c depicts the non-dimensional required supply pressure p^*_s versus $\dot{m}$. We can observe that the curtailed sample yields a higher supply pressure despite having a dwindled jet spreading. In other words, the jet spreading effectiveness θ^*_{max}/p^*_s is noticeably higher for the longer actuator.

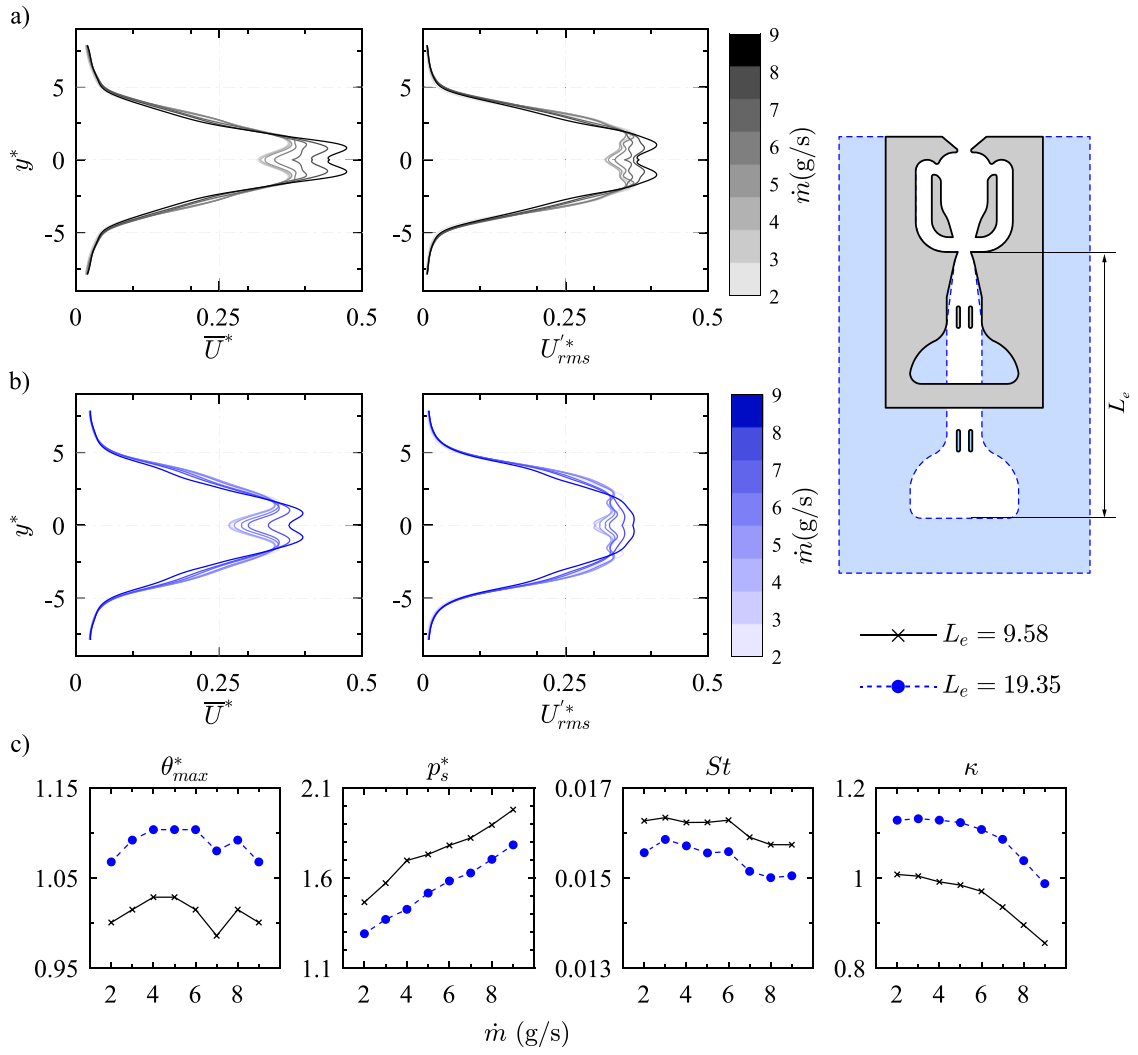

Fig. 3. (a) The non-dimensional mean velocity profiles $\overline{U}^*(y^*)$, (b) the non-dimensional RMS velocity profiles $U'^*_{rms}(y^*)$, and (c) performance parameters: the non-dimensional jet deflection angle θ^*_{max}, the non-dimensional required supply pressure p^*_s, Strouhal number St, and the jet switching quality κ of actuators with different entrance length L_e for $\dot{m}$ = 2–9 g/s at x^* = 2.52.

The SWJ oscillation frequency is another fluidic oscillator's critical performance parameter. The SWJ oscillation frequency is automatically detected from the PSDs using the FindPeaks function in Matlab 2022a Signal Processing Toolbox. f_0 is the sweeping jet fundamental frequency and f_1, f_2 and f_3 are the harmonics. We can estimate the Strouhal number of the actuator as $St = f_0 d_{hyd}/\overline{U}_{in}$. The average Strouhal number for the milled actuator (S_a = 0.2 μm) is $St \approx 0.0161$, which corroborates the St values of a milled actuator reported in the literature [53]. Fig. 3c shows the Strouhal number versus $\dot{m}$ for different entrance length L_e. We can see that the shorter actuator yields a higher oscillation frequency due to diminished jet spreading.

For a wide range of applications, including flow control and heat transfer enhancement, the jet switching quality κ is another crucial performance parameter that quantifies the unsteady nature of the sweeping jet and the amount of disturbance created. κ is defined as the ratio of the unsteady momentum input to the steady momentum:

$$\kappa = \frac{U'_{rms}(y^*)}{\overline{U}(y^*)} \tag{3}$$

Where $\overline{U}(y^*)$ is the mean of the velocity profiles and $U'_{rms}(y^*)$ is the mean of the root mean square (RMS) velocity fluctuation profiles at $x^* = 2.52$ and $y^* = 0$. In other words, κ measures the sweeping jet turbulence intensity, and the fluidic oscillator with a higher κ effectuates a more energy-efficient flow control [54]. We can see that the actuator with L_e = 19.35 yields a higher jet switching quality due to an elevated unsteady momentum evident from $U'_{rms}(y^*)$ profile.

As presented above, the general performance of the shortened actuator is degraded compared to the original design, and the efficiency with respect to supply pressure requirements suffers a penalty of 10% to 20%. Nevertheless, from the additive manufacturing point of view, this downsizing results in reducing the printing time by 54% and lowering the actuator mass and cost by 63.2% in the example of printer P_1. In our experiment, where the focus is on the comparative performance of different actuators and their raster angles, absolute performance values are irrelevant, which justifies the trade-off.

3.2. The impact of 3D printing raster angle

This section presents the results related to the 3D printing raster angle. Fig. 4a–c depict the non-dimensional mean velocity $\overline{U}^*(y^*)$ for $\dot{m}$ = 3, 6 and 9 g/s at x^* = 2.52 for printers P_1, P_2 and P_3. Regardless of the surface roughness values and the raster angle, for all printers, the mean velocity profiles feature a bifurcated profile typical for this type of SWJ actuator, albeit with a drastic reduction in jet spreading for 45

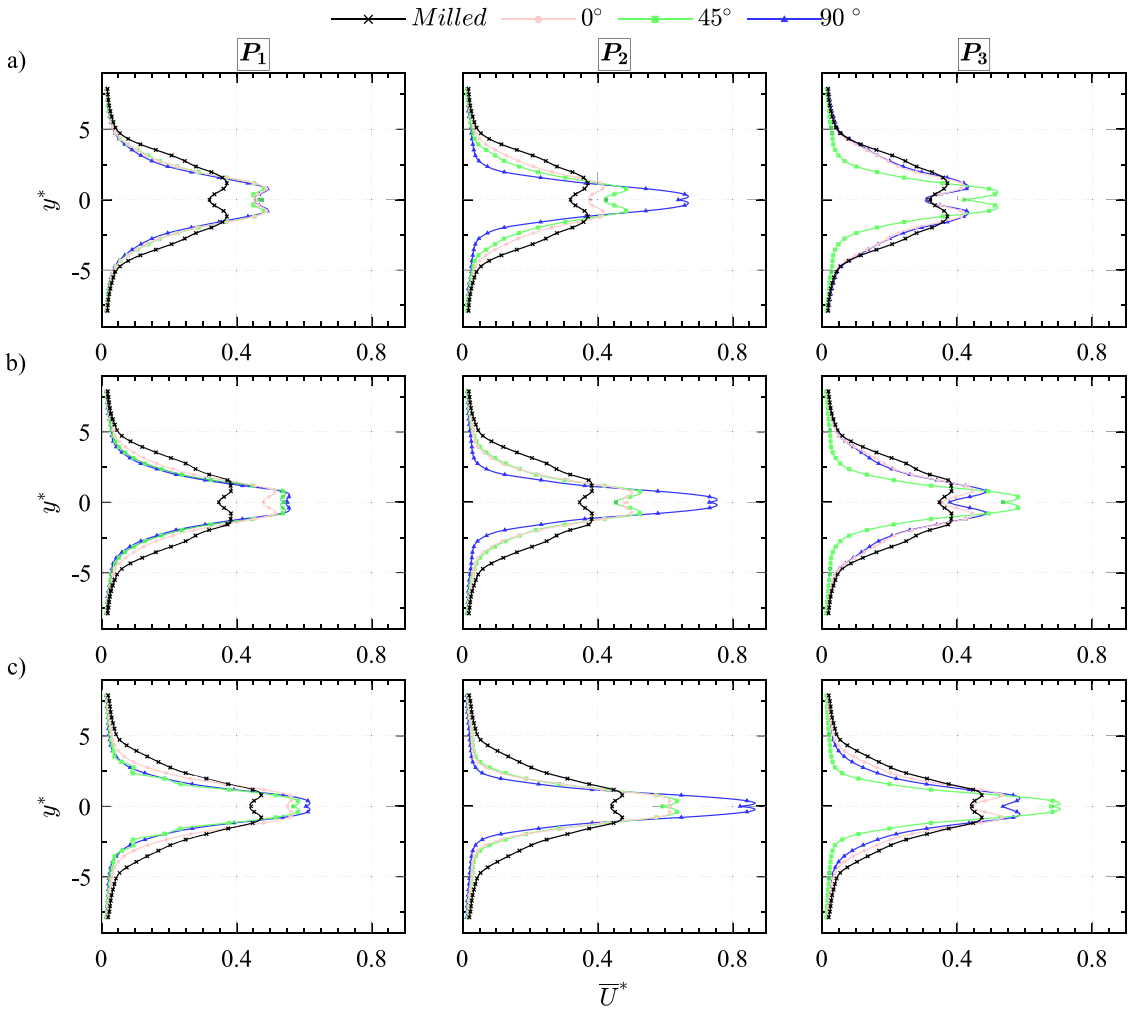

Fig. 4. The non-dimensional mean velocity profiles $\overline{U}^*(y^*)$ of actuators with different raster angle for printers P_1, P_2, and P_3 for (a) $\dot{m} = 3$ g/s, (b) $\dot{m} = 6$ g/s, and (c) $\dot{m} = 9$ g/s at $x^* = 2.52$.

and 90°, more pronounced for P_2^{90} and P_3^{45}. Thus, the raster angle and associated increased surface roughness do not change the jet's external flow regime [51].

It is interesting to note that for parts produced by printer P_3, the velocity at the center line of the actuator ($y^* = 0$) is equivalent to the milled actuator, albeit with a higher maximum velocity U_{max} at the twin peaks, indicating a longer dwelling time at maximum jet deflection angle. This can be further corroborated by the RMS velocity profiles shown in Fig. 5a, featuring a similar distribution where the unsteady momentum U'^*_{rms} for P_3^0 and P_3^{90} is higher compared to the milled actuator. This can be advantageous for flow control applications where higher turbulence intensity is desirable.

Fig. 5b depicts the PSDs of $U'(t, 2.36)$ for 3D printer actuators versus raster angle, for $\dot{m} = 3$ g/s at $x^* = 2.52$. The amplitude and definition of the oscillation frequency peaks are directly related to the jet deflection angle [51]. We can note that for printed actuators, the fundamental and first harmonic frequency peaks are not as sharply defined as in the case of the milled sample, more noticeably for raster angles 45 and 90°.

Similar to the machined actuator, Fig. 6 depicts the main performance parameters for different printers for varying raster angles. The maximum jet deflection angle θ^*_{max} is shown in Fig. 6a for printers P_1, P_2 and P_3. We note that the printed samples effectuate a lower θ^*_{max} compared to the milled actuator for all tested raster angles. For printer P_1, a raster angle of 0° yields a higher jet deflection. It can be noted that θ^*_{max} for 0° is higher than $\alpha = 45°$ despite having a higher surface roughness. As mentioned in Section 2.1, for printer P_1, the actuators exhibit a clear raster angle pattern. Due to this surface texture, the jet deflection θ^*_{max} does not monotonically reduce with the increase in surface roughness S_a. In a similar vein, for printer P_2, the surface texture feature a well-defined raster angle pattern and hence, $\alpha = 0°$ outperforms 90° for all tested mass flow rates and yields higher θ^*_{max} than $\alpha = 45°$ for $\dot{m} = 2$ and 3 g/s.

On the other hand, actuators produced by printer P_3 do not manifest a clearly-defined raster angle pattern. P_3^{90} yield equivalent jet spreading to $\alpha = 0°$ except for $\dot{m} = 8$ and 9 g/s, despite having twice surface roughness value compared to 0°. However, for this printer, similar to printers P_1 and P_2, we note that 0° raster angle outperforms 45° for all tested mass flow rates.

As shown in Fig. 6b, for the additive manufactured samples, the required supply pressure p^*_s is lower than the machined actuator despite having rougher surfaces. This can be attributed to drastically diminished jet spreading for the printed actuators. In other words, the required supply pressure p^*_s is related to the jet spreading θ^*_{max} [51]. For the milled piece with $S_a = 0.2$ μm, the required supply pressure ranges from $1.46 \leq p^*_s \leq 1.98$ whereas 3D printed oscillators provoke a noticeably smaller variation in supply pressure for $\dot{m} = 2$ and 9 g/s.

Fig. 6c depicts the Strouhal number versus inlet mass flow rate for different printers at varying raster angles. Typically, the sweeping jet

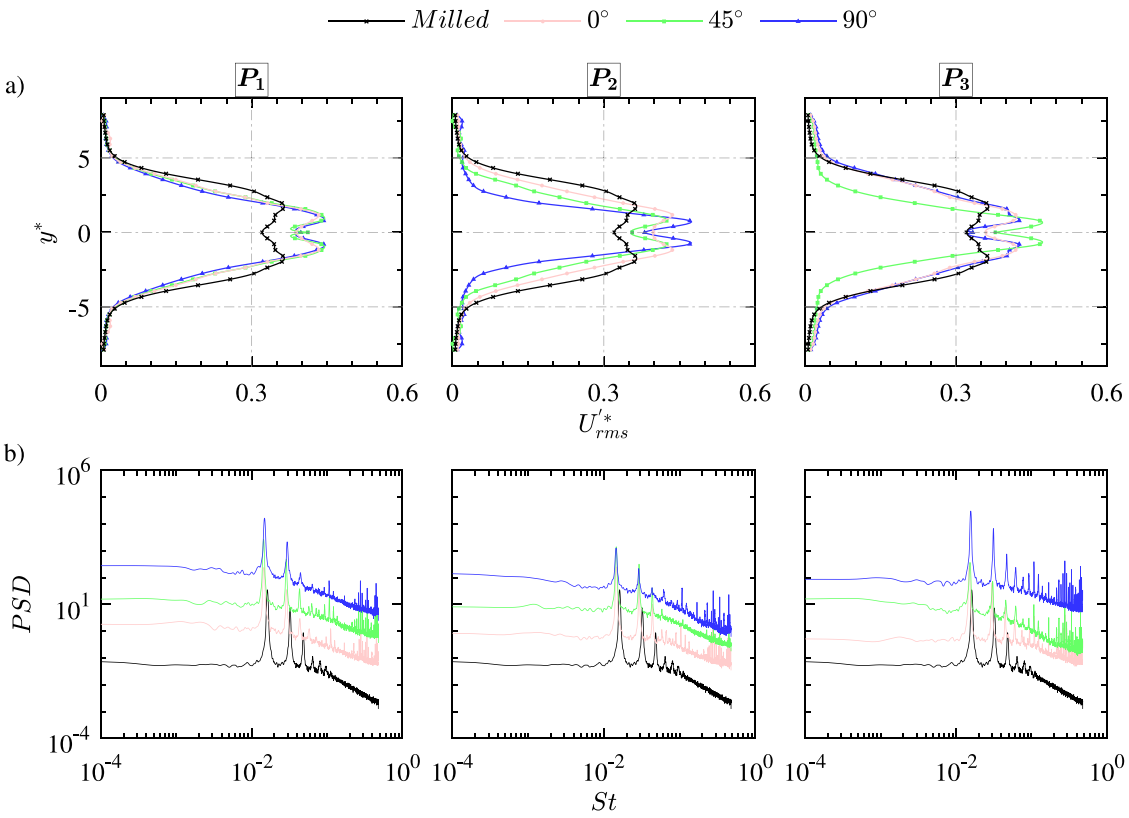

Fig. 5. (a) The non-dimensional RMS velocity profiles $U'^*_{rms}(y^*)$ and (b) PSDs of $U'(t, 2.36)$ (in log–log scale, amplitudes shifted by a decade for clarity) of actuators with different raster angle for printers P_1, P_2, and P_3 for $\dot{m} = 3$ g/s at $x^* = 2.52$.

oscillation frequency or the associated Strouhal number is inversely proportional to the jet deflection angle θ^*_{max}. Analogous to a simple pendulum oscillatory motion, the jet oscillation frequency ought to increase with the reduction in jet spreading, provided all other factors remain intact [51].

Nonetheless, we can note that for all printed samples except for P_2^{90}, P_3^{45} and P_3^{90} at $\dot{m} = 9$ g/s, the Strouhal number is lower than the milled actuator. This can be attributed to the deviation in the main geometric features for the printed actuators, as summarized in Table 1. For instance, the oscillation frequency drops with the increase in depth h, which is the case for printer P_1 samples. Also, as shown in Fig. 3c, a higher turbulence intensity results in a lower jet oscillation frequency. The added roughness leads to a shorter hydrodynamics entry length [55], resulting in a higher turbulence intensity for some of the 3D printed pieces, and hence, the jet oscillation frequency drops.

Fig. 6d shows the jet switching quality κ for varying raster angles using different 3D printers. It can be observed that for printer P_1, the jet switching quality κ experiences a similar trend to the jet deflection. Likewise, for printer P_2, κ is lower than the milled sample except for 0° raster angle at lower $\dot{m}$ values. For printer P_3, 45° raster angle yields lower jet switching quality values for all the mass flow rates, while strikingly, for $\alpha = 0$ and 90°, the jet switching quality is higher than milled actuator that can be attributed to the entrance region. Alternatively stated, the added roughness for P_3^0 and P_3^{90} results in a shorter hydrodynamic entry region [55] compared to the smooth milled surface. Therefore, for applications where higher turbulence intensity fluidic actuation is required, additive manufactured samples with a surface texture similar to P_3^0 and P_3^{90} can be considered as an alternative with significantly lower required supply pressure.

The increased jet spreading typically results in higher required supply pressure. We investigate the relationship between supply pressure p_s^* and the maximum jet deflection angle θ^*_{max} shown in Fig. 7. It can be noticed that the milled actuator yields a higher supply pressure demand as a result of higher jet spreading and a larger recirculation bubble in the mixing chamber [53]. Among the printed samples with various raster angles, there is a large overlap. Nonetheless, the data points related to 0° are on the higher side, and the required supply pressure for 90° is generally lower, more noticeably for P_1 and P_2.

Fig. 8 shows the relationships between the normalized maximum jet deflection angle θ^*_{max} versus the surface roughness S_a at different raster angle $\alpha = 0$, 45, and 90°. The power-law fits are presented for the three tested raster angles. Table 2 summarize the coefficients of power-law fit $\theta^*_{max} = C + A(S_a)^B$ with 90% confidence bounds for different raster angle. We can note that for $\alpha = 90°$, the data points related to P_3 with $S_a = 22.3$ μm are entirely outside the prediction bounds. These fits are meant to provide a rough estimation of the jet spreading for each raster angle. However, the estimate is only applicable when a clear raster angle pattern is present on the surface, as in the cases of actuators P_1 and P_2 (see Fig. 2). When the pattern is at $\alpha = 0°$, the progression of θ^*_{max} versus the surface roughness S_a approaches a linear trend which was observed in [44] for varying homogeneous surface roughness. This implies that a raster angle of $\alpha = 0°$ impacts the flow less dramatically, which could be plausibly expected. On the other hand, larger raster angles diminish the importance of surface roughness and impose a highly non-linear (power-law) trend. Here, actuator P_3 is an outlier; it features a pattern which is very inconsistent between the different raster angles, as evidenced in Fig. 2. This inconsistency yields a different behavior in Fig. 8 with respect to the power law.

4. Conclusions

The impact of raster angle from FDM-based 3D printing on the fluidic oscillator flow and energy characteristics is investigated experimentally. The resulting performance is assessed in terms of the jet's external properties and actuator's overall energy efficiency for an extended range of inlet mass flow rates $\dot{m} = 2$–9 g/s. The performance

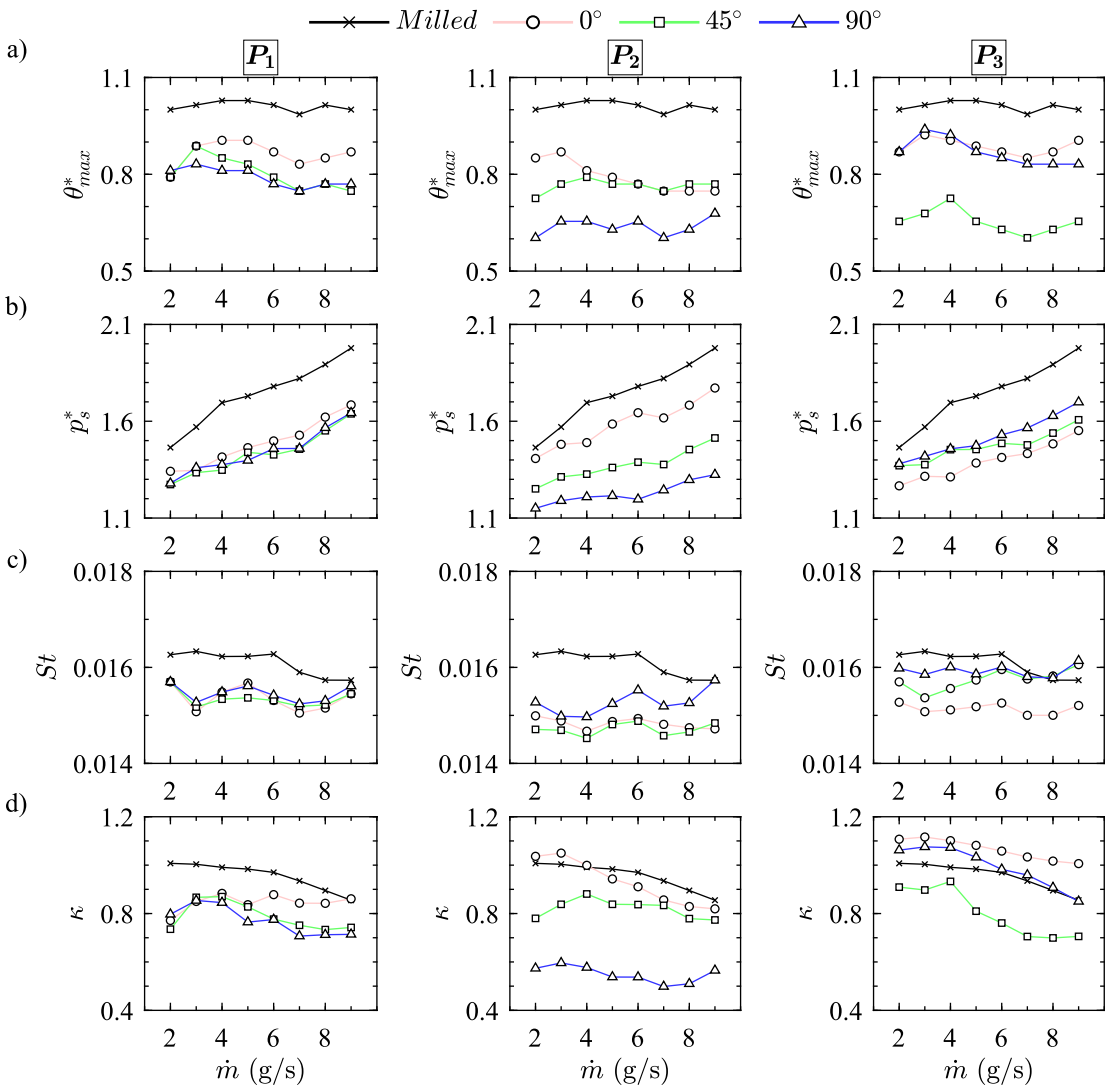

Fig. 6. Flow properties of actuators versus $\dot{m}$ for printers P_1, P_2, and P_3 at different raster angle $\alpha = 0$, 45 and 90°: (a) the non-dimensional maximum jet deflection angle θ^*_{max}, (b) the non-dimensional required supply pressure p^*_s, (c) Strouhal number St, and (d) the jet switching quality κ.

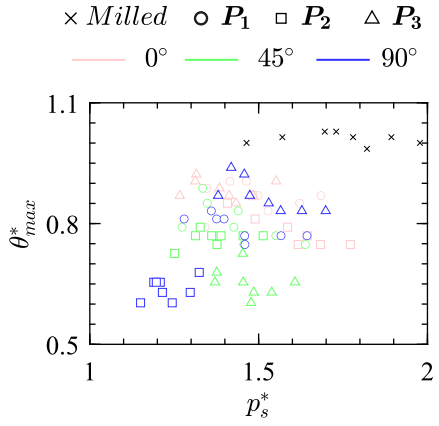

Fig. 7. Relationship between the non-dimensional required supply pressure p^*_s and the non-dimensional maximum jet deflection angle θ^*_{max}. The respective raster angle and printer is indicated in the legend.

of a smooth machined sample is compared with 3D printed samples with raster angles of 0, 45, and 90° from three different 3D printers.

Printing at different raster angles resulted in remarkably dissimilar surface finishes, and therefore, the actuator's overall performance was significantly impacted. It is observed that for all the three tested printers, 0° raster angle yields the closest performance to the machined actuator, which can be considered the optimal printing raster angle while raster angle $\alpha = 45°$ must be avoided. The striking result is that for the oscillator with an indistinct raster direction pattern, despite having a higher surface roughness, the performance is remarkably enhanced, more noticeably for $\alpha = 90°$. Thus, it may be recommended that the pattern associated with the raster angle be removed using different post-processing methods such as blasting and chemical etching. The presented power-laws can be used as a rough estimation of jet spreading θ^*_{max} versus surface roughness for different raster angles $\alpha = 0$, 45 and 90°.

We can conclude that by closely examining the surface morphology, actuators produced through FDM-based additive manufacturing must be characterized extensively in terms of main performance parameters. Future studies should be conducted considering other operational parameters of FDM-based 3D printing, such as air gap, the orientation of printing, and raster width. Multi-objective optimization is imperative to precisely estimate the significance level of individual factors and identify interactions between various input parameters with respect to the surface texture and, ultimately, concerning the fluidic oscillator performance parameters.

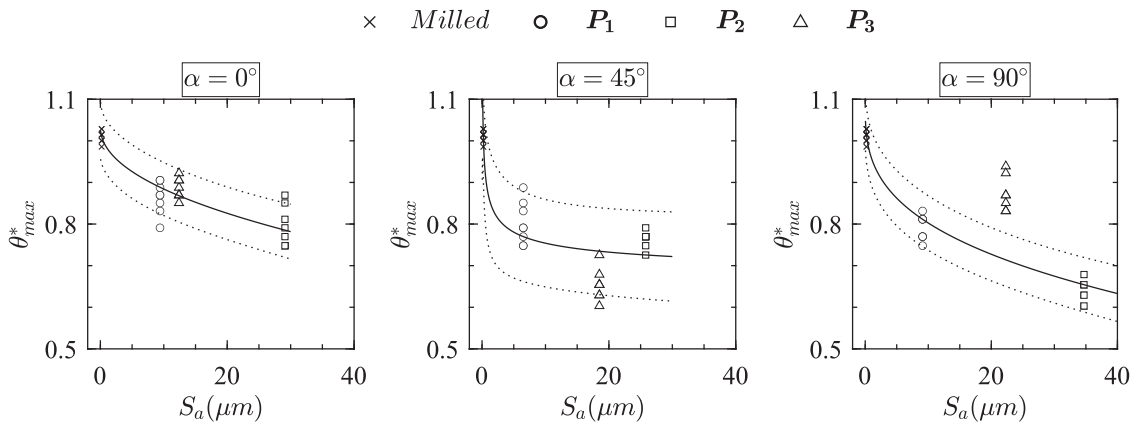

Fig. 8. Relationships between the normalized maximum jet deflection angle θ^*_{max} versus the surface roughness S_a at different raster angle $\alpha = 0$, 45 and 90°. The solid line is the fitted power-law, and the dashed lines depict 90% prediction bounds. The respective printer is indicated in the legend on the top.

Table 2
The coefficients of the power-law fit with 90% confidence bounds for different raster angle α.

α	A	B	C
0°	−0.050(−0.099, −0.001)	0.474(0.223, 0.725)	1.034(0.983, 1.085)
45°	0.227(−0.169, 0.623)	−0.307(−0.862, 0.247)	0.642(0.321, 0.963)
90°	−0.137(−0.241, −0.033)	0.33(0.166, 0.492)	1.095(0.998, 1.192)

Declaration of competing interest

The authors declare that they have no known competing financial interests or personal relationships that could have appeared to influence the work reported in this paper.

Data availability

Data will be made available on request.

Acknowledgments

This publication is based upon work supported by the Khalifa University of Science and Technology under Award No. CIRA-2019-025. The authors would like to thank the KU staff, especially R. Ganithi and S. Bojanampati, for their exceptional support in this experiment.

References

[1] Z.A. Qureshi, E. Elnajjar, O. Al-Ketan, R.A. Al-Rub, S.B. Al-Omari, Heat transfer performance of a finned metal foam-phase change material (FMF-PCM) system incorporating triply periodic minimal surfaces (TPMS), Int. J. Heat Mass Transfer 170 (2021) 121001.

[2] Z.A. Qureshi, S.A.B. Al-Omari, E. Elnajjar, O. Al-Ketan, R.A. Al-Rub, On the effect of porosity and functional grading of 3D printable triply periodic minimal surface (TPMS) based architected lattices embedded with a phase change material, Int. J. Heat Mass Transfer 183 (2022) 122111.

[3] M. Modrek, A. Viswanath, K.A. Khan, M.I.H. Ali, R.K.A. Al-Rub, An optimization case study to design additively manufacturable porous heat sinks based on triply periodic minimal surface (TPMS) lattices, Case Stud. Therm. Eng. 36 (2022) 102161.

[4] M. Alteneiji, M.I.H. Ali, K.A. Khan, R.K.A. Al-Rub, Heat transfer effectiveness characteristics maps for additively manufactured TPMS compact heat exchangers, Energy Storage Saving 1 (3) (2022) 153–161.

[5] K. Kara, D. Kim, P.J. Morris, Flow-separation control using sweeping jet actuator, AIAA J. 56 (11) (2018) 4604–4613.

[6] T. Crittenden, S. Raghu, Combustion powered actuator with integrated high frequency oscillator, Int. J. Flow Control 1 (1) (2009) 87–97.

[7] O. Agwu, A. Valera-Medina, Diesel/syngas co-combustion in a swirl-stabilised gas turbine combustor, Int. J. Thermofluids 3–4 (2020) 100026.

[8] A.R. Tajik, T. Shamim, A.F. Ghoniem, R.K.A. Al-Rub, The impact of critical operational parameters on the performance of the aluminum anode baking furnace, J. Energy Resources Technol. 143 (6) (2020).

[9] P. Nakate, D. Lahaye, C. Vuik, The nitric oxide formation in anode baking furnace through numerical modeling, Int. J. Thermofluids 12 (2021) 100122.

[10] T. Hussain, M. Talibi, R. Balachandran, Impact of local secondary gas addition on the dynamics of self-excited ethylene flames, Int. J. Thermofluids 9 (2021) 100057.

[11] A.A. Ezzi, M.A. Fayad, A.M.A. Jubori, A.A. Jaber, L.A. Alsadawi, H.A. Dhahad, M.T. Chaichan, T. Yusaf, Influence of fuel injection pressure and RME on combustion, NO emissions and soot nanoparticles characteristics in common-rail HSDI diesel engine, Int. J. Thermofluids 15 (2022) 100173.

[12] M. Laimon, T. Yusaf, T. Mai, S. Goh, W. Alrefae, A systems thinking approach to address sustainability challenges to the energy sector, Int. J. Thermofluids 15 (2022) 100161.

[13] S. Soleimani, S. Eckels, A review of drag reduction and heat transfer enhancement by riblet surfaces in closed and open channel flow, Int. J. Thermofluids 9 (2021) 100053.

[14] M. Kadivar, D. Tormey, G. McGranaghan, A review on turbulent flow over rough surfaces: Fundamentals and theories, Int. J. Thermofluids 10 (2021) 100077.

[15] M. Metka, J.W. Gregory, Drag reduction on the 25-deg Ahmed model using fluidic oscillators, J. Fluids Eng. 137 (5) (2015).

[16] D. Veerasamy, A.R. Tajik, L. Pastur, V. Parezanović, Effect of base blowing by a large-scale fluidic oscillator on the bistable wake behind a flat-back Ahmed body, Phys. Fluids 34 (3) (2022) 035115.

[17] X. Chen, S. Zhong, O. Ozer, A. Weightman, Control of afterbody vortices from a slanted-base cylinder using sweeping jets, Phys. Fluids 34 (7) (2022) 075115.

[18] T.I. Khan, A.R. Tajik, V. Parezanovic, Drag reduction of a generic transport vehicle model using a fluidic oscillator, Int. J. Thermofluids (2022) 100180.

[19] A.R. Kadam, A.R. Tajik, V. Hindasageri, Heat transfer distribution of impinging flame and air jets – A comparative study, Appl. Therm. Eng. 92 (2016) 42–49.

[20] R. Kempers, J. Colenbrander, W. Tan, R. Chen, A. Robinson, Experimental characterization of a hybrid impinging microjet-microchannel heat sink fabricated using high-volume metal additive manufacturing, Int. J. Thermofluids 5–6 (2020) 100029.

[21] A.R. Tajik, T. Shamim, A.F. Ghoniem, R.K.A. Al-Rub, CFD modelling of NOx and soot formation in aluminum anode baking furnace, in: Volume 8A: Heat Transfer and Thermal Engineering, Vol. 52118, American Society of Mechanical Engineers, 2018, V08AT10A016.

[22] A. Jacob, K. Shafi, K. Roy, Heat transfer characteristics of piston-driven synthetic jet, Int. J. Thermofluids 11 (2021) 100104.

[23] S.N. Diop, B. Dieng, A. Warore, S. Mbodj, A study on heat transfer characteristics by impinging jet within a few amounts of mist, Int. J. Thermofluids 13 (2022) 100130.

[24] T.O. Onah, B.N. Ekwueme, A.O. Odukwe, N.B. Nduka, A.C. Orga, M.O. Egwuagu, S. Chukwujindu, C. Diyoke, M.A. Nwankwo, C.T. Asogwa, C.C. Aka, K.O. Enebe, C.O. Asadu, Improved design and comparative evaluation of controlled water jet impingement cooling system for hot-rolled steel plates, Int. J. Thermofluids 15 (2022) 100172.

[25] D. Ravi, T.K.R. Rajagopal, Numerical investigation on the effect of geometric shape and outlet angle of a bladeless fan for flow optimization using CFD techniques, Int. J. Thermofluids (2022) 100174.

[26] T.I. Khan, V. Parezanović, L. Pastur, O. Cadot, Suppression of the wake steady asymmetry of an Ahmed body by central base bleed, Phys. Rev. Fluids 7 (8) (2022) 083902.
[27] T. Park, K. Kara, D. Kim, Flow structure and heat transfer of a sweeping jet impinging on a flat wall, Int. J. Heat Mass Transfer 124 (2018) 920–928.
[28] Y. Wu, S. Yu, L. Zuo, Large eddy simulation analysis of the heat transfer enhancement using self-oscillating fluidic oscillators, Int. J. Heat Mass Transfer 131 (2019) 463–471.
[29] A. Serrar, M. El Khlifi, A. Kourta, Characterisation and comparison of unsteady actuators: A fluidic oscillator and a sweeping jet, Internat. J. Numer. Methods Heat Fluid Flow (2021).
[30] V. Hindasageri, P. Kuntikana, A.R. Tajik, R.P. Vedula, S.V. Prabhu, Axis switching in impinging premixed methane-air flame jets, Appl. Therm. Eng. 107 (2016) 144–153.
[31] M. Zaidani, R.A. Al-Rub, A.R. Tajik, T. Shamim, Computational modeling of the effect of flue-wall deformation on the carbon anode quality for aluminum production, in: Heat Transfer Summer Conference, 57885, American Society of Mechanical Engineers, 2017, V001T02A010.
[32] A.R. Tajik, T. Shamim, A.F. Ghoniem, R.K.A. Al-Rub, Multi-objective optimization of aluminum anode baking process employing a response surface methodology, Energy Procedia 158 (2019) 5541–5550.
[33] S. Mohammadshahi, H. Samsam-Khayani, T. Cai, K.C. Kim, Experimental and numerical study on flow characteristics and heat transfer of an oscillating jet in a channel, Int. J. Heat Fluid Flow 86 (2020) 108701.
[34] M. Grandemange, O. Cadot, M. Gohlke, Reflectional symmetry breaking of the separated flow over three-dimensional bluff bodies, Phys. Rev. E 86 (3) (2012).
[35] O. Cadot, M. Almarzooqi, A. Legeai, V. Parezanović, L. Pastur, On three-dimensional bluff body wake symmetry breaking with free-stream turbulence and residual asymmetry, C. R. Mecanique 348 (6–7) (2020) 509–517.
[36] E.-C. Hsu, L. Pastur, O. Cadot, V. Parezanović, A fundamental link between steady asymmetry and separation length in the wake of a 3D square-back body, Exp. Fluids 62 (5) (2021).
[37] I. Afgan, Y. Kahil, S. Benhamadouche, P. Sagaut, Large eddy simulation of the flow around single and two side-by-side cylinders at subcritical Reynolds numbers, Phys. Fluids 23 (7) (2011) 075101.
[38] I. Afgan, C. Moulinec, D. Laurence, Numerical simulation of generic side mirror of a car using large eddy simulation with polyhedral meshes, Internat. J. Numer. Methods Fluids 56 (8) (2008) 1107–1113.
[39] N. Abed, I. Afgan, A CFD study of flow quantities and heat transfer by changing a vertical to diameter ratio and horizontal to diameter ratio in inline tube banks using URANS turbulence models, Int. Commun. Heat Mass Transfer 89 (2017) 18–30.
[40] V. Parezanović, R. Monchaux, O. Cadot, Characterization of the turbulent bistable flow regime of a 2D bluff body wake disturbed by a small control cylinder, Exp. Fluids 56 (1) (2015).
[41] J. McDonough, R. Law, J. Kraemer, A. Harvey, Effect of geometrical parameters on flow-switching frequencies in 3D printed fluidic oscillators containing different liquids, Chem. Eng. Res. Des. 117 (2017) 228–239.
[42] M.A. Hossain, A. Ameri, J.W. Gregory, J. Bons, Effects of fluidic oscillator nozzle angle on the flowfield and impingement heat transfer, AIAA J. 59 (6) (2021) 2113–2125.
[43] I. Kaur, P. Singh, State-of-the-art in heat exchanger additive manufacturing, Int. J. Heat Mass Transfer 178 (2021) 121600.
[44] A.R. Tajik, V. Parezanović, Additive manufacturing impact on a fluidic oscillator with respect to surface roughness, Int. J. Heat Fluid Flow 97 (2022) 109040.
[45] S. Masood, Advances in fused deposition modeling, in: Comprehensive Materials Processing, Elsevier, 2014, pp. 69–91.
[46] S. Gupta, A. Bit, Rapid prototyping for polymeric gels, in: Polymeric Gels, Elsevier, 2018, pp. 397–439.
[47] H. Gonabadi, Y. Chen, A. Yadav, S. Bull, Investigation of the effect of raster angle, build orientation, and infill density on the elastic response of 3D printed parts using finite element microstructural modeling and homogenization techniques, Int. J. Adv. Manuf. Technol. 118 (5–6) (2021) 1485–1510.
[48] J. Black, DeGarmo's Materials and Processes in Manufacturing, Wiley, Hoboken, 2019.
[49] B. He, S. Ding, Z. Shi, Metrology and Measurement Systems, Polish Academy of Sciences Committee on Metrology and Scientific Instrumentation, 2021.
[50] B.Z. Slupski, K. Kara, V. Parezanovic, D. Kyritsis, Experimental inner pressure analysis of a sweeping jet actuator, in: 2018 Applied Aerodynamics Conference, American Institute of Aeronautics and Astronautics, 2018.
[51] A.R. Tajik, K. Kara, V. Parezanović, Sensitivity of a fluidic oscillator to modifications of feedback channel and mixing chamber geometry, Exp. Fluids 62 (12) (2021).
[52] R. Woszidlo, F. Ostermann, C.N. Nayeri, C.O. Paschereit, The time-resolved natural flow field of a fluidic oscillator, Exp. Fluids 56 (6) (2015).
[53] R. Woszidlo, F. Ostermann, H.-J. Schmidt, Fundamental properties of fluidic oscillators for flow control applications, AIAA J. 57 (3) (2019) 978–992.
[54] D. Schatzman, J. Wilson, E. Arad, A. Seifert, T. Shtendel, Drag-reduction mechanisms of suction-and-oscillatory-blowing flow control, AIAA J. 52 (11) (2014) 2491–2505.
[55] H. Li, Y. Li, B. Huang, T. Xu, Flow characteristics of the entrance region with roughness effect within rectangular microchannels, Micromachines 11 (1) (2019) 30.